A TID and SEE Radiation-Hardened, Wideband, Low-Noise Amplifier

Benjamin Mossawir, *Student Member, IEEE*, Ivan R. Linscott, *Member, IEEE*, Umran S. Inan, *Fellow, IEEE*, James L. Roeder, Jon V. Osborn, *Member, IEEE*, Steven C. Witczak, *Member, IEEE*, Everett E. King, *Member, IEEE*, and Stephen D. LaLumondiere, *Member, IEEE*

***Abstract*—We have developed a radiation-hardened, highly linear, wideband, low-noise amplifier (LNA) with programmable gain to serve as the front-end of a plasma-wave instrument for satellite-based electric-field measurements of very low frequency (VLF) phenomena in the Van Allen radiation belts. Fabricated in a commercial 0.25-μm silicon-germanium BiCMOS process, this ASIC leverages radiation-hardness-by-design techniques at the topological, implementation, and layout levels to maintain 75-dB spurious-free dynamic range (SFDR) over nearly four decades of frequency, from 100 Hz to 1 MHz, for both proton and γ-ray total ionizing dose (TID) exposures up to 1000 krad(Si). Single-event effect (SEE) testing via pulsed laser confirms negligible latchup sensitivity and suppression of single-event transients (SETs) at the output for beam energy LET equivalents in excess of 100 MeV-cm^2/mg in even the most sensitive regions of the die.**

***Index Terms*—BiCMOS, feedback, harmonic distortion, large-signal linearity, plasma waves, radiation hardening, spurious-free dynamic range, VLF receivers, wideband amplifiers.**

I. Introduction

RECENTLY, efforts to investigate the nature of wave particle interactions within the Van Allen belts of the Earth's magnetosphere have intensified [1], [2]. However, this region is especially inhospitable to high-fidelity scientific instrumentation on account of the strong doses of ionizing radiation to which circuits are exposed as a result of large populations of trapped energetic particles [3].

In particular, plasma-wave receivers for in-situ electric-field measurements must withstand such particle fluxes while still capturing signatures of impulsive natural phenomena over much of the ULF-MF portion of the spectrum (100 Hz–1 MHz) with sufficient linearity and dynamic range to support spectrographic resolution of weak emissions such as upper hybrid waves (with power spectral densities, or PSDs, on the order of 10 nV/m/$\sqrt{\text{Hz}}$) in the presence of strong ones such as chorus (on the order of 100 μV/m/$\sqrt{\text{Hz}}$), as seen in Fig. 1.

Manuscript received July 15, 2006; revised September 5, 2006. This work was supported in part by NASA under Advanced Technology Grant NAG5-10822 at Stanford University and the Aerospace Corporation.

B. Mossawir, I. R. Linscott, and U. S. Inan are with the Department of Electrical Engineering, Stanford University, Stanford, CA 94305-9505 USA (e-mail: bmoss@stanford.edu).

J. L. Roeder is with the Space Science Applications Laboratory, The Aerospace Corporation, Los Angeles, CA 90009-2957 USA.

J. V. Osborn, S. C. Witczak, E. E. King, and S. D. LaLumondiere are with the Electronics and Photonics Laboratory, The Aerospace Corporation, Los Angeles, CA 90009-2957 USA.

Digital Object Identifier 10.1109/TNS.2006.886219

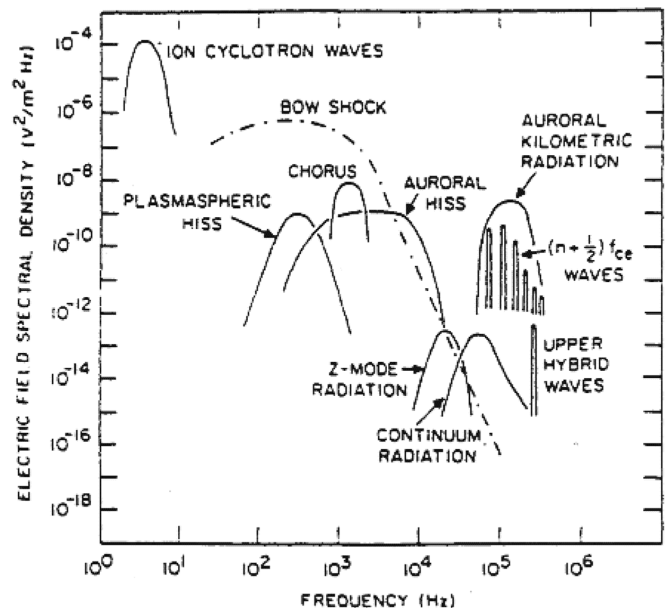

Fig. 1. Representative plasma wave phenomena justifying wide bandwidth and dynamic range of proposed receiver. Reproduced/modified by permission of American Geophysical Union [4].

To process inputs spanning nearly four (five) decades in frequency (magnitude) [4], conventional receivers partition both ranges, taking the form of either multi-channel spectrum analyzers [5] or sweep frequency receivers [6] to address the former, and employing low dynamic range amplifiers with automatic gain control [7] to accommodate the latter.

This work demonstrates a custom, integrated low-noise amplifier (LNA) whose wide bandwidth and linear dynamic range enable a receiver with the unique ability to process the full complement of these wave phenomena simultaneously. In addition to facilitating scientific objectives unrestrained by the independent and piecewise nature of previous solutions, such an amplifier presages the ability to conduct interferometric experiments via clusters of nano-satellites made possible by its lower mass and power consumption.

Achieving specifications that match or surpass those of existing receivers (Table I), over a lifetime in a typical Van Allen belt orbit, with its concomitant total ionizing dose (TID) degradation due to proton and γ-ray exposure (at a projected level of 100 krad(Si)/yr) and the single-event effects (SEE) generated by high-energy particle incidence, constitutes the primary design challenge addressed in this paper. Sections II and III describe the circuit architecture and implementation with partic-

0018-9499/$20.00 © 2006 IEEE

TABLE I
SELECTED LNA ELECTRICAL SPECIFICATIONS

Symbol	Parameter	Min	Typ	Max	Unit
A_V	Voltage Gain	0		20	dB
SFDR	Linear Dynamic Range[a]		75		dB
THD	Harmonic Distortion		70		dB
ΔV_{out}	Allowable Output Swing[b]	0.35	0.9	1.45	V
f_p	-3dB Output Bandwidth	10^{-1}		10^3	kHz
P_{avg}	Average Power Dissipation		750		μW

[a]In the context of spectrographic on-board data analysis, dynamic range is computed as a spot quantity, not integrated over full system bandwidth.
[b]Applies to differential half-circuit; quantities are measured single-ended.

ular emphasis on hardening techniques employed. Sections IV and V present the measured performance of the prototype LNA for TID and SEE irradiations, respectively.

II. HARDENING-BY-ARCHITECTURE

A. Manufacturing Process

To achieve the stringent SFDR specifications at the low end of the input signal bandwidth, which translate to a noise PSD of 100 nV/$\sqrt{}$Hz at 100 Hz for a nominal 10-m dipole antenna, the LNA signal path must be constructed largely from npn bipolar junction transistors (BJTs). These exhibit lower $1/f$ noise corners and coefficients than their lateral pnp and MOS counterparts [8], [9] which are subject to the random trapping and de-trapping of carriers at the $Si\text{-}SiO_2$ interface due to their surface current conduction [10]. Indeed, corners in excess of 1 MHz render many modern CMOS processes impractical.

However, it is also desirable to have access to native MOSFETs in the process so as to support the possibility of future integration of the LNA with an analog-to-digital converter (ADC) to form a single-chip receiver. Coupled with the inherent robustness of the smaller device cross-sections for modern feature sizes [11] and the proven intrinsic hardness of SiGe HBTs [12], these requirements justify the use of a commercial BiCMOS manufacturing process—National Semiconductor's 0.25-μm SiGe BiCMOS.

B. LNA Topology

To realize a passband gain whose accuracy remains stable over the lifetime of the part, so that the standard error of the measured data is consistent, even as the gain itself is programmed between 0–20 dB, the LNA cannot assume an open-loop topology. Instead, the dependence of the LNA gain accuracy on both small-signal parameters of its forward path active elements, which degrade under radiation, and the magnitude of the loop transmission, which varies by a factor of 10 over the 0–20 dB tuning range, must be minimized.

To wit, let the LNA take the form of a generalized single-loop feedback system and consider the elementary application of Mason's gain rule which yields the well-known expression for $A(s)$, the closed-loop system gain, as

$$A(s) = \frac{a}{1+af} = \frac{a}{1+L} \approx \frac{1}{f}. \quad (1)$$

When the approximation in (1) is valid, (i.e., when the loop transmission, L, which is the product of the open-loop gain a and feedback factor f, is much larger than unity), passive feedback is an effective technique for reducing the system sensitivity to open-loop gain variations caused by radiation-induced degradation of transistors in the forward path [13].

However, that sensitivity, which represents gain error due to δa, varies with respect to the forward path gain according to

$$\frac{\delta^2 A(s)}{\delta a^2} = \frac{-2f}{(1+af)^3} \approx \frac{-2}{aL^2}. \quad (2)$$

So, once the open-loop gain has dropped by just 10%, a value in line with the TID transistor degradation to be discussed in Section III, the sensitivity will be 37% more dependent on the transistor amplification properties. Likewise, this dependence is inversely proportional to the square of the loop transmission, so that at the highest LNA gain settings, the changes in gain error due to transistor degradation will be 100 times larger. Thus, single-loop feedback alone cannot correct for drift in the measurement uncertainty over the part lifetime.

Instead, we must augment the passive outer feedback loop with an active inner feedback loop around the transistors that generate a, such that the sensitivity of the open-loop gain, and thus the magnitude of the associated δa under radiation, is significantly reduced. In essence, the active feedback ensures that, independent of changes in value of f for the purpose of gain programming, the large loop transmission required to make the approximation in (1) is provided by a stable a.

To realize this strategy, the topology of the LNA is adapted from [14], which heavily leverages passive feedback to provide linear operation over a wide input signal range in the context of instrumentation amplifiers. A simplified schematic of the modified amplifier is shown in Fig. 2.

Emitter-followers Q_1–Q_4 compose the nominal forward path, a, around which the connection of resistors R_D and $R_L = R_{L1} + R_{L2}$ provides passive feedback to set the overall gain as:

$$A(s) \approx \frac{1}{f} = \frac{R_L}{R_D}. \quad (3)$$

The additional active feedback loop is provided by differential pairs M_1/M_3 and M_2/M_4 which, in canonical single-loop architectures, would be current mirrors. By connecting the gates of M_1 and M_2 to the collectors of Q_1 and Q_2 instead, converting the latter into super emitter-followers [13], this topology extends the classic approach of merely shifting the burden of robustness to the passives in f. It establishes an insensitive forward-path gain, a, and hence L, as well.

III. HARDENING-BY-IMPLEMENTATION

A. Linearity

Even with both these architectural advantages, hardness-by-design at the implementation level is necessary to meet the demanding linearity specifications. Consider the case of the ideal common-emitter (CE) amplifier in Fig. 3(a), operating in the large-signal regime where $v_{BE} = V_{BE} + v_{be}$

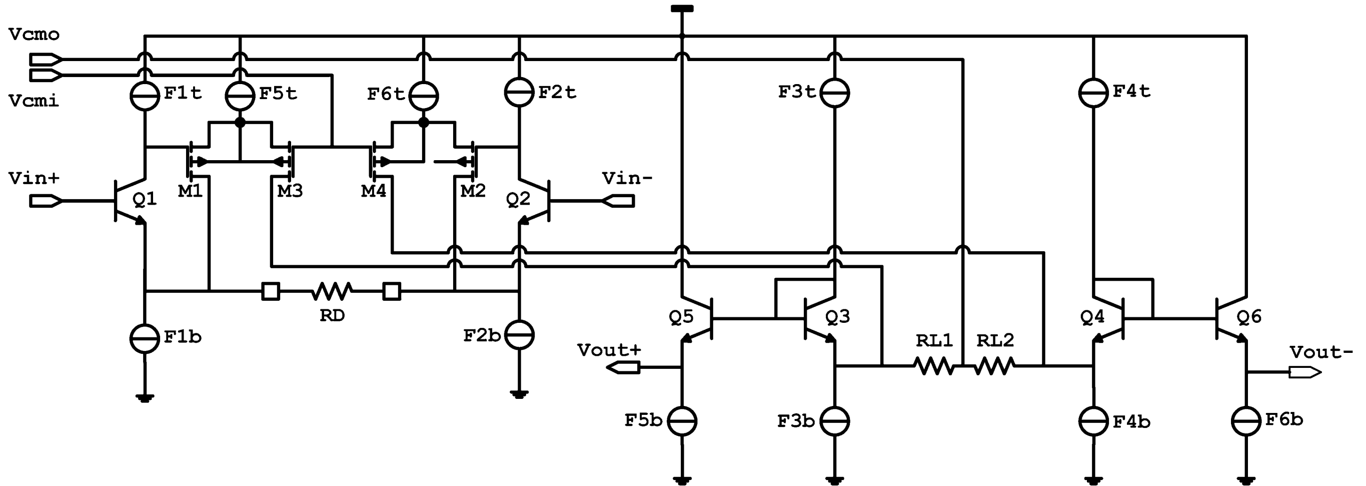

Fig. 2. Simplified schematic of LNA topology, adapted from [14], highlighting both active and passive feedback loops.

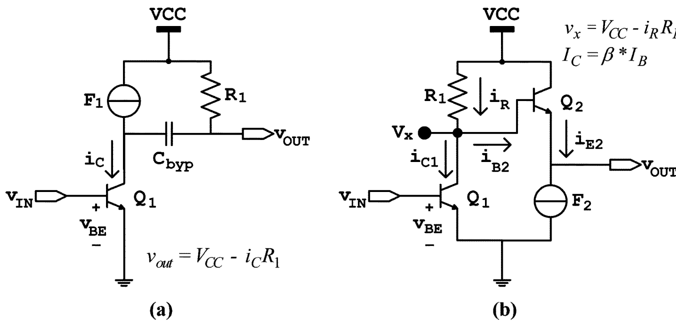

Fig. 3. Large-signal representations of (a) canonical CE amplifier and (b) CE–EF cascade. Load on $V_{\rm out}$ not pictured in either case.

and $i_C = I_C + i_c$. At sinusoidal steady-state, the gain-determining I–V relationship, which is given by

$$I_C + i_c = I_S e^{V_{BE}/nV_T} e^{v_{be}/nV_T}, \qquad (4)$$

holds over several decades of i_C, making the bipolar transistor apropos for amplification subject to the large-signal linearity requirements of this application. Truncating the Taylor expansions of the exponentials in (4) for a sinusoidal input of the form $v_{be} = v_i * \cos(\omega_o t)$, yields the ratio of the magnitude of the third harmonic to the fundamental, which typically dictates the overall SFDR in any well-designed differential system, as:

$$\frac{|H(j*3\omega_o)|}{|H(j*\omega_o)|} = \frac{|v_{be}|^2}{24n^2V_T^2} = \frac{1}{24}\ln^2\left(\frac{|i_c|}{I_s}\right). \qquad (5)$$

Since the sensitivity of this result to the amplitude of the output sinusoid, i_c, which can be easily derived as

$$\gamma = \frac{1}{12}\frac{I_S}{i_c} ln\left(\frac{i_c}{I_S}\right), \qquad (6)$$

does not depend on the collector bias current, I_C, we may conclude that signal-independent changes in I_C, such as those which result from radiation-induced g_m-degradation of the devices that compose F_1, are not likely to violate the SFDR specifications (presuming sufficient margin and matching).

However, the same is not true of signal-dependent i_C variations. Consider the simple common-emitter/emitter-follower (CE–EF) cascade in Fig. 3(b), exemplary of the typical interface between successive stages of a multi-stage amplifier. As $v_{\rm OUT}$ swings, i_{E2} will vary by i_{e2} in order to drive the subsequent load. Mitigated by β_2, this same variation is reflected in the base current of Q_2 and hence appears at the first stage output, $v_X = V_{CC} - i_R * R_1$, according to: $i_R = i_{C1} + i_{B2} \approx i_{C1} + i_{E2}/\beta_2$. So, in addition to the desired i_{c1} there is now a signal-dependent component to the overall Q_1 output, i_{e2}/β_2, whose size depends on β_2—a radiation-susceptible parameter. According to (5), the SFDR of the first stage will thus depend on the radiation-induced β-degradation of the second.

To assess the severity of this β-degradation, and hence the importance of such inter-stage nonlinear dependencies, we irradiated a series of npn process-test devices up to 1 Mrad(Si) using γ-ray radiation from a ^{60}Co source. In Fig. 4 we have extracted the variations in β from the Gummel plots and isolated the percent change of its peak value as a function of total dose. The nearly -18% change in the peak current gain at 1 Mrad(Si) will result in substantial non-linear inter-stage coupling according to the mechanism described above. Extending this effect to a cascade of such stages, it can be shown that its cumulative impact renders the target SFDR of the overall amplifier unattainable.

Our solution is to employ a novel design method wherein we abandon the transconductance of the BJTs and operate them only as voltage-mode devices, thereby escaping their inherently non-linear characteristic. Similarly, MOSFETs are employed purely as current-mode elements, wherein their ideal current gain from drain-to-source is leveraged to perform lossless summing operations. This cedes all V-to-I and I-to-V conversions to the most linear elements available—resistors.

Several features of the implementation in Fig. 2 evidence this strategy. The independent specification of both I_E and I_C for the input emitter-follower pair (Q_1/Q_2) assures that the current density of these devices remains fixed across the entire

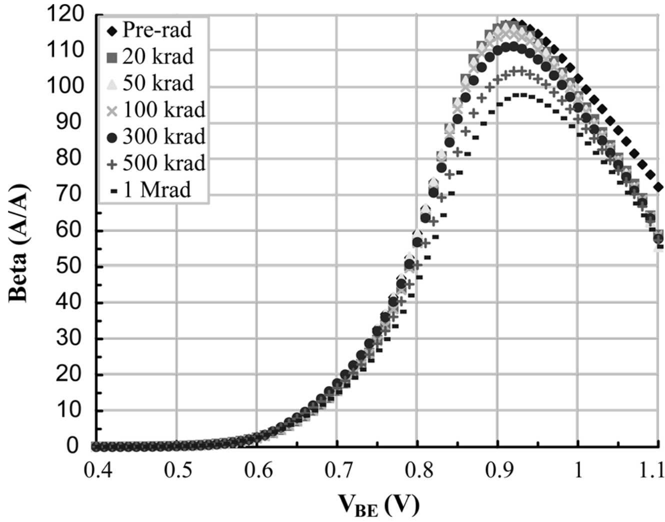

Fig. 4. β-vs-V_{BE} curves for representative CBE npn transistor ($A_e = 0.4 \times 0.7\ \mu m^2$) at several doses. At 1 Mrad(Si), β has dropped by $\approx -18\%$.

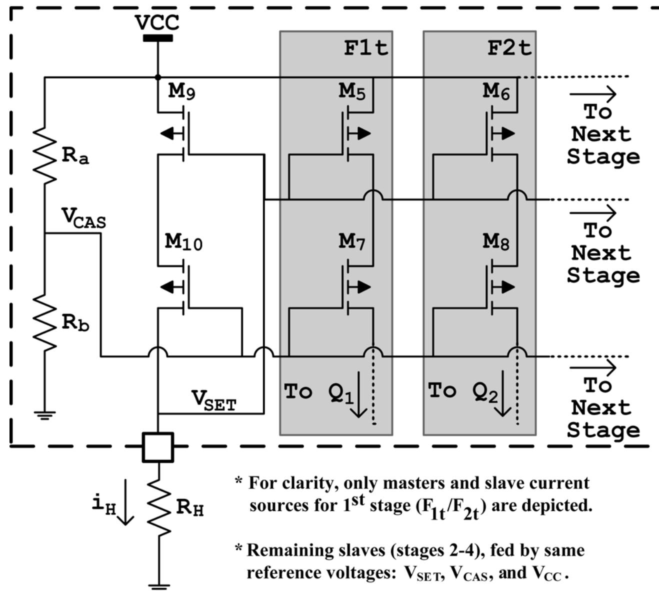

Fig. 5. Implementation of top-rail bias current generators and stage biasing. Master reference current I_H is set by combination of R_H, and M_1.

input range, improving linearity by avoiding any traversal of their β-vs-v_{BE} curve (e.g., Fig. 4) with input signal variations. A similar technique is employed in the third stage to improve the linearity of the voltage shift through Q_3/Q_4. Notably, the use of pMOS devices M_1–M_4 to fold the current from the first stage to the third, as opposed to the lateral pnps used in [14], affords several advantages. Among them, by not siphoning signal-dependent i_B away from Q_1/Q_2, they preserve the linearity of the first stage better than even a Darlington pair.

B. Power Dissipation

In this design, the principal causes of increased demand for supply current with total dose exposure are variations in the threshold voltage (V_{TH}) and transconductance (g_m) of the MOS elements responsible for reference generation. The top-rail current sources in Fig. 2 (F_{1t}–F_{6t}) are implemented as low-voltage cascodes in which the master reference current is determined by an off-chip resistor and the gate-bias of the cascode devices set by an on-chip resistor ladder. (Fig. 5).

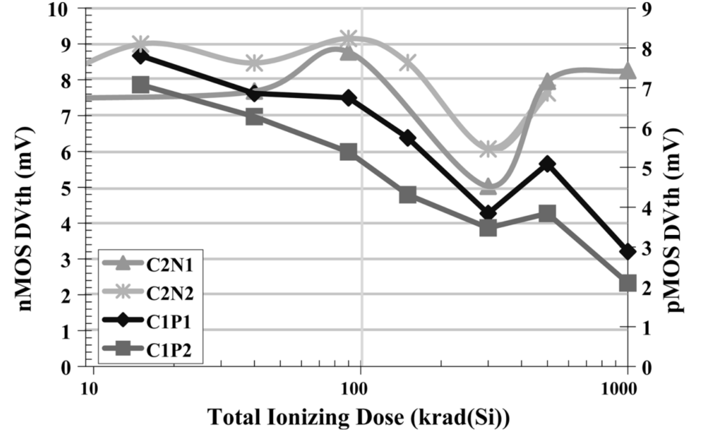

Fig. 6. Measured threshold voltage variations, ΔV_{TH}, of 34.88-μm/0.24-μm common-centroid nMOS and pMOS pairs for ^{60}Co γ-ray exposure up to 1 Mrad(Si). During irradiation devices are biased with worst-case V_{GS} of 2.5 V for nMOS, 0 V for pMOS. nMOS ΔV_{TH} shows classic rebound.

Consider diode M_9, which mirrors the off-chip reference current I_H to each of the slaves (M_5, M_6, etc.), ignoring for the moment the effect of cascode device M_{10}. Using a small-signal model to assess the dependence of I_H on the radiation-induced degradation of its transconductance yields the simple relation

$$I_H = \frac{V_{CC}}{\frac{1}{g_{m9}} + R_H}. \tag{7}$$

Since the nominal value of V_{SET} is chosen to lie near the midpoint of the supply, $V_{CC}/2$, we can conclude that the master reference current will scale roughly in proportion to g_{m9}.

By contrast, the dependence of I_H on the variations of V_{TH9} is best visualized through a load-line analysis in which a square-law model of M_9 is sufficient since all bias devices have $L \geq 1\ \mu m$. This yields the following pair of expressions,

$$I_H = \frac{1}{2}\mu_n C_{OX}\left(\frac{W}{L}\right)_9 (V_{GS9} - V_{\mathrm{TH9}})^2, \tag{8a}$$

$$V_{GS9} = V_{CC} - I_H R_H. \tag{8b}$$

The location of the operating point depends in a sub-linear fashion on the translation of the parabola in (8a) along the V_{GS9} axis. Thus, the sensitivity of I_H to δV_{TH9} is much less severe than to δg_{m9}. For typical MOSFET model parameters, deviations of $\pm 10\%$ in V_{TH9} change I_H by only $\approx \pm 3.7\%$.

Given the relative prominence of these dependencies, we characterized the ^{60}Co γ-ray susceptibility of a series of MOS devices on the aforementioned test vehicles to determine which flavor should be used in conjunction with R_H in Fig. 5, in light of their respective V_{TH} and g_m degradation profiles.

Fig. 6 depicts the radiation-induced change in the V_{TH} of representative common-centroid pairs of nMOS and pMOS devices under worst-case bias conditions for the build-up of oxide trapped charge near the Si-SiO$_2$ interface. According to (8), the rise in nMOS V_{TH} above 200 krad(Si) will produce an undesirable drop in drain current. In contrast, for pMOS pair $C_1P_1/C_1P_2, \Delta V_{\mathrm{TH}}$ exhibits a nearly monotonic trend.

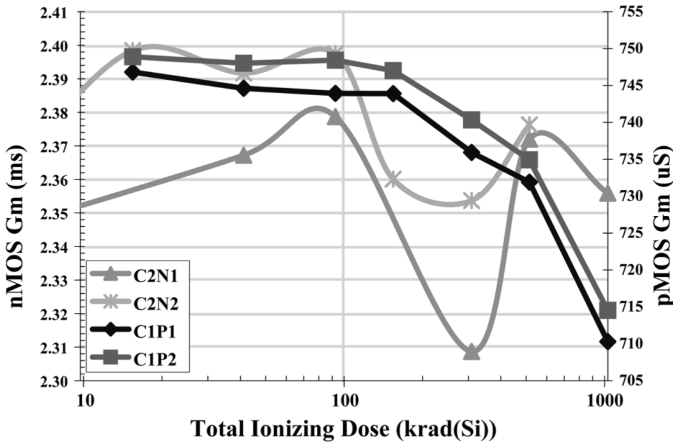

Fig. 7. Measured g_m of same MOS pairs as in Fig. 6 for ^{60}Co γ-ray exposure up to 1 Mrad(Si). pMOS g_m is more well-behaved, exhibiting steady decline up to -5.35% at 1 Mrad(Si) due to mobility degradation.

As it is contrary to theory, the negative slope of this change merits further investigation given that only one pMOS pair was characterized, whereas the nMOS ΔV_{TH} behavior was confirmed for multiple samples. However, it clearly renders these pMOS devices superior for ΔV_{TH}-sensitive bias circuits.

Fig. 7 assesses the additional impact of mobility degradation due to the build up of interface states by examining the variation in maximum g_m for the same MOS samples. Despite the smaller total extent of its deviations over the full TID range, the nMOS response is less robust on account of the undulations, which can lead to increased supply current when the transconductance peaks, according to (7).

Given the gradual decay of the pMOS ΔV_{TH} and g_m responses, and in spite of the large absolute changes they exhibit up to 1 Mrad(Si), we choose to implement M_9 with a pMOS device rather than nMOS since the current draw of the diode-connected configuration depends critically on the value of g_m. This choice guarantees I_H, and hence overall LNA power dissipation, will not grow as TID damage accumulates.

Whereas the design of the diode-connected biasing elements relies on g_m-degradation to limit power dissipation, we utilize benign pMOS threshold variations to establish V_{CAS}, via an on-chip resistor ladder in the form of R_a and R_b, since ΔV_{TH} figures more prominently when gate voltage is fixed.

C. Transient Response

Fig. 8 exemplifies the conscientious layout practices adopted to mitigate the single-event latchup (SEL) drawbacks of using a BiCMOS technology. Substrate-tap rings [15] and nested minority carrier guard rings [16] are placed around critical homogeneous arrays. Though not conferring absolute immunity to arbitrary LETs, these inhibit the efficiency of the parasitic thyristor feedback loop by reducing the values of the diffusion resistances and β's of the undesired bipolar devices.

Fortuitously, the same layout techniques sedulously applied to reduce device mismatch differential systems, such as spatial locality, common-centroid arrays, and dummy devices [16], also prove effective in rejecting single-event transients (SETs)

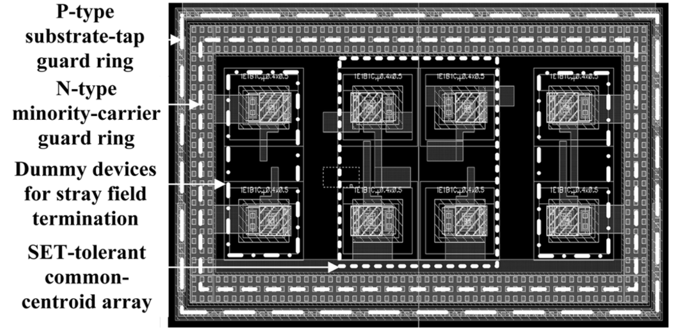

Fig. 8. Layout example of LNA input devices Q_1/Q_2. Demonstrates SEL mitigation techniques, such as nested guard rings, and SET suppression by means of maximum differential proximity.

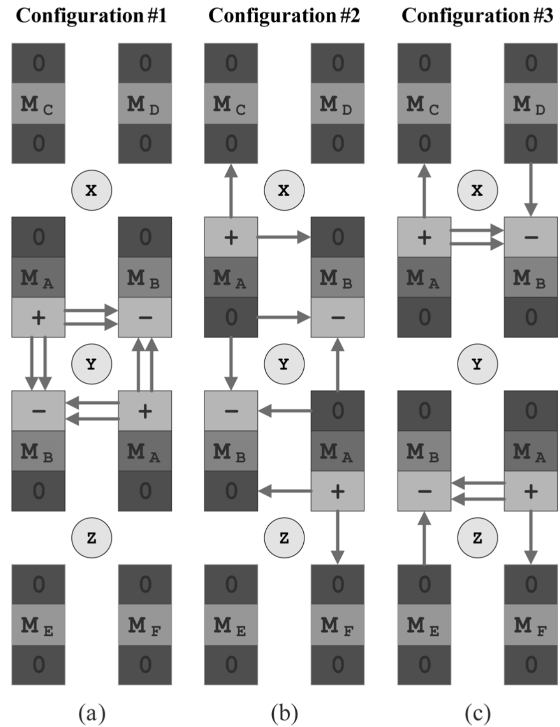

Fig. 9. Comparison of drift E-field profiles for SET-tolerant common-centroid layouts of pMOS differential pair. Strike occurs at X, Y, or Z when polarity of output signal is such that drain of M_A (M_B) is positive (negative) relative to common source node (0). Configuration #1 yields highest expected value of differential transient amplitude but lowest incidence rate.

by increasing the likelihood that they appear as common-mode disturbances.

Consider the 2-D common-centroid layouts of a pMOS differential pair (M_A/M_B) in Fig. 9. Though all will cancel the effects of arbitrary 1-dimensonal doping gradients, the choice of terminal orientation affects the polarity of the transients induced by deposited charge. In the situation depicted, a hypothetical strike occurs at the center of the array (Y) when the signal being processed by the differential pair is driving the drain of M_A (M_B) high (low). The field lines of #1 will tend to funnel the negative (positive) charge from the central strike toward M_A (M_B). The resulting output transients of will be of opposite polarity, and thus not differentially cancelled. Configuration #2 is somewhat better, with fields of half the strength, while #3 is optimal since there is no preferred drift direction for the charge.

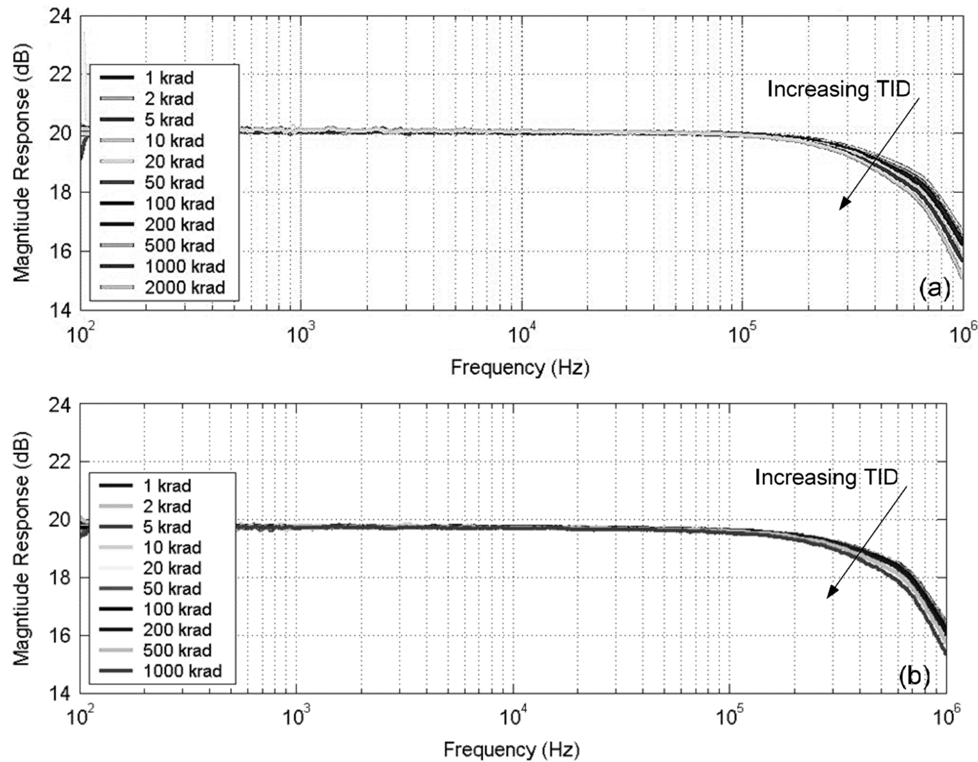

Fig. 10. Bode magnitude responses of LNA versus TID for (a) γ-ray and (b) H^+ sources. DC gain and passband ripple vary negligibly up to 1000 krad(Si) in both cases. Bandwidth compression, which results from reduced power consumption, also tracks regardless of radiation source.

Repeating this analysis at locations X and Z reveals that, in terms of the expected value of the transients resulting from a random strike, the configurations can be ranked in order of ascending preference as 1–3–2. However, since our upset rate is essentially independent of SET amplitude, given the high dynamic range, we prefer #1 because it only results in differential SETs $1/3$ of the time.

Thus, to minimize SET probability, the LNA layout adopts such terminal orientations, where possible, so that free charge will not drift preferentially toward one device. Note that the presence of neighboring dummies at fixed potential (M_C–M_F) is a prerequisite for this and similar arguments concerning uniform field terminations, so they are also deployed liberally.

IV. TID Results

To confirm the effectiveness of our hardness-by-design techniques, a prototype of the LNA was fabricated and subjected to total dose irradiation in both a ^{60}Co chamber and a high-energy proton beam. Both sources applied the same logarithmic (1, 2, 5) dose steps from 1 to 2000 krad(Si). At the 2000 krad(Si) step of the proton irradiation, the part abruptly failed, exhibiting a sharp drop in supply current and railed outputs. Pending further tests to duplicate this failure signature on additional samples, data from this step has been omitted.

A. Experimental Set-Up

The γ-ray irradiation was performed using the chamber in [17] to illuminate the part with a pair of 3500Ci ^{60}Co rods. For all experiments, the bias board was housed in a Pb-Al box compliant with method 1019.6 of [18] to minimize dose-rate enhancement from scattered, low-energy photons. Since ELDRS is known to be highly process-dependent [19] and the prototype was manufactured on an inchoate line, a high dose rate of 75 rad/s calibrated to $\pm 5\%$ is appropriate for this work.

TABLE II
Proton Irradiation Dose Steps

Total Dose krad(Si)	Avg. Time s	Avg. Flux P/cm^2-s	Avg. Dose Rate rad(Si)/s
≤ 20	573	4.08x10^7	6.80
50	1500	1.20x10^8	20.00
100	319	9.40x10^8	156.76
≥ 200	1939	1.51x10^9	252.33

To reduce exposure duration, beam flux was manually enhanced prior to each of the 50, 100, and 200 krad(Si) dose steps.

Proton irradiations were performed with the 88” Cyclotron at Lawrence Berkeley National Laboratory (LBNL). A standard beam energy of 50 MeV was used throughout. To reduce exposure durations for the highest dose steps, the beam flux was incrementally scaled according to Table II.

In both cases, a single instance of the LNA was irradiated under nominal bias conditions and a programmed gain of 14 dB, but without input. Between dose steps, an automated series of measurements, lasting $\sim$45 minutes, characterized the device performance at a programmed gain of 20 dB.

B. Frequency Response

Cumulative Bode magnitude plots of the LNA frequency response for both TID irradiation sources are displayed in Fig. 10. Fig. 11 extracts the changes in critical parameters

Fig. 11. Normalized (a) DC gain and (b) 3-dB bandwidth of Bode responses in Fig. 12. The sensitivity of (b) in response to npn and pMOS transistor degradation confirms the effectiveness of techniques behind the robustness evidenced in (a).

of these curves as a function of dose and normalizes each to eliminate slight differences in absolute value that arise from chip-to-chip variation. Regardless of the radiation source, the DC gain is accurate to ± 0.05 dB up to 1 Mrad(Si), and the flatness of the passband gain as a function of frequency, as measured by the 3σ ripple (not pictured), is preserved to within 0.19 dB over the same range. Similarly, the drop in the 3-dB bandwidth at 1 Mrad(Si) TID is approximately -15% for both cases. The strong agreement of this data confirms that the predominant TID damage mechanisms consist of interface states and oxide trapped charge. The displacement damage unique to the H^+ exposure has no measurable effect on the LNA frequency response.

Although the passband gain of Fig. 11 is quite immune, and within specification, the sizable 3-dB bandwidth compression merits further explanation. It reflects the reduction of the non-dominant pole, p_2, which, it can be shown, is governed to first order, for a differential capacitive load C_1 at the output (not shown), by

$$p_2 = \frac{1}{2C_l[(g_{m_{7,8}})^{-1} + (g_{m_{5,6}}(\beta_{7,8}+1))^{-1}]} \approx \frac{(\beta_{7,8}+1)I_{C_{5,6}}}{2C_l V_T}, \tag{9}$$

where $\beta_{7,8}$ is the current gain of followers Q_7 and Q_8 in Fig. 2, and $I_{c5,6}$ is the nominal collector bias current of followers Q_5 Q_{6*}. Recognizing that the non-dominant pole is proportional to $(\beta+1)I_C$, its behavior is readily explained by considering the degradation of both quantities at 1 Mrad(Si) according to Figs. 4 and 7, respectively, namely

$$\frac{p_2|_{1000\ \mathrm{krad}}}{p_2|_{0\ \mathrm{krad}}} \propto \left(\frac{\beta|_{1000\ \mathrm{krad}}+1}{\beta|_{0\ \mathrm{krad}}+1}\right)\left(\frac{I_C|_{1000\ \mathrm{krad}}}{I_C|_{0\ \mathrm{krad}}}\right) \approx 0.861. \tag{10}$$

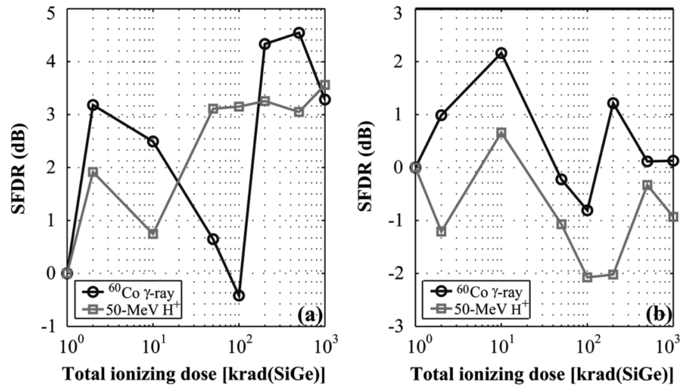

Fig. 12. Normalized SFDR for ^{60}Co and γ-ray exposures up to 1 Mrad(Si) using 37.4 mV_{pp} input tones with (a) 1 kHz and (b) 10 kHz fundamentals. No statistically significant dose dependence is evident.

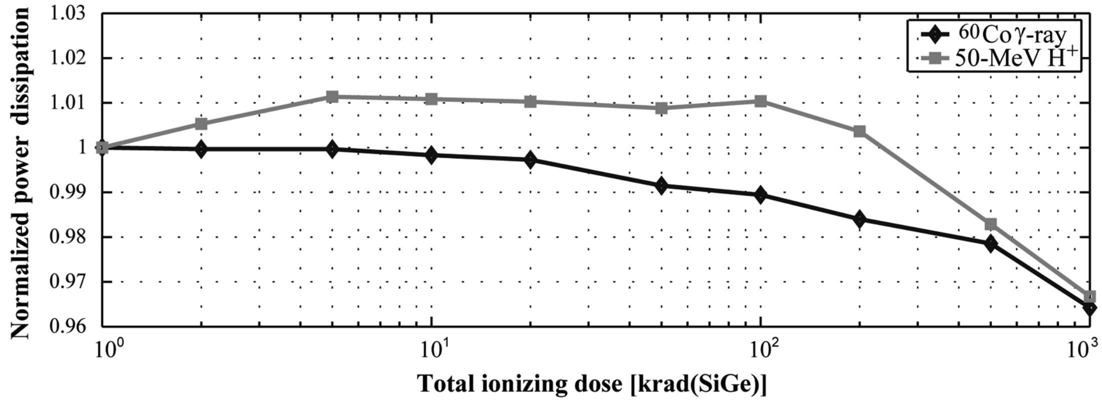

Fig. 13. Normalized maximum power dissipation for ^{60}Co and γ-ray exposures up to 1000 krad(Si), as measured before thermal equilibrium is achieved. The drop in power follows from design of the reference generation circuitry to conservatively incorporate pMOS g_m-degradation.

Thus, the roughly -15% bandwidth compression results from a combination of pMOS g_m-degradation, which reduces the power dissipation via bias current I_C, and npn β-degradation.

Whereas this phenomenon reveals the radiation-induced change in the parameters of both underlying transistor flavors, we see no corresponding change in the passband quantities, confirming that our architectural hardening techniques are indeed effective in mitigating the dependence of DC gain on the active devices, even for significant parameter shifts.

C. Linearity

To examine the efficacy of the techniques described in Section III.A for maintaining highly linear operation, a series of single-tone tests was performed at multiple amplitudes and fundamental frequencies. For two cases where the undesirable harmonics are most pronounced (37.4 $\mathrm{mV_{pp}}$ input tones at 1 kHz and 10 kHz) the SFDR is normalized by it pre-rad value and plotted in Fig. 12 as a function of dose for both sources.

More illuminating than the absolute distortion levels, on the order of 75-dB (73-dB) SFDR for the 1 kHz (10 kHz) input, is the lack of any declining trend. Granted, these patterns are commingled with a measurement standard error for spectral power of ± 2 dB that reflects both the uncertainty introduced by environmental noise being amplified by the LNA and, to a lesser extent, the approximations of the parabolic interpolation used for peak height estimation. However, mutual correlation of data from both radiation sources breeds confidence that the harmonic fidelity is uncorrelated with TID up to 1 Mrad (Si).

Thus, we have successfully decoupled the overall amplifier linearity from inter-stage loading that depends on β-degradation which is sensitive to either γ-ray or H^+ radiation.

D. Power Dissipation

Fig. 13 confirms that the LNA does not demand additional supply current as it succumbs to TID effects. Its total power draw, including the demands of the reference voltage and current pins, was sampled at the outset of the automated test suite, before those demands were able relax as it reached thermal equilibrium. Data sets from both radiation sources are consistent in showcasing the efficacy of the vigilant biasing described in Section III.B—the maximum supply current at 1 Mad(Si) is lower by an average of -3.48%.

TABLE III
PROPERTIES OF PULSED LASER

Symbol	Property	Value	Notes
W	Pulse width	15ps	Full-width, half-maximum
P_O	Average power	0.04 mW	Beam energy $E_O = P_O * f_P$
f_P	Pulse rate	1 MHz	R6G dye cavity dump rate
f_O	Repetition rate	100 Hz	Electro-optical shutter rate

No correction is applied to account for area of die metallization openings.

Since the drop in supply current is precipitated by the g_m-degradation of the pMOS diodes that systematically mirror the master reference current to the bias branches of each stage, it is directly responsible for the bandwidth compression observed in Fig. 11, via the I_C term in (9). The astute observer will note that the percent change in supply current at 1 Mrad(Si) is slightly less than that of the pMOS g_m-degradation purported to be its underlying cause (-5.35% as characterized in Fig. 9(b)), despite the proportionality professed in (7). This results from a simplification in the schematic of Fig. 6 where the current through R_H is returned to ground. In practice, it is returned to on-chip npn diodes, whose effect is to replace the linear function in Fig. 7 with an exponential and thereby mitigate the master current reduction via negative feedback.

V. SEE Results

To verify performance with respect to both SEL and SET sensitivity, the prototype was scanned with a picosecond-pulsed laser, via a well-known method [20], [21]. The spatial resolution ($\sim$1 μm) and penetration depth ($\sim$1.8 μm) of the chosen λ permit the identification and characterization of the sensitive junctions and cross-sections, but their probative value is constrained by the extent of die metal coverage.

A. Experimental Set-Up

SEE scans were performed with the 590-nm, actively mode-locked, cavity-dumped dye laser in [22]. A series of calibrated neutral density filters was used to vary the beam intensity whose transmittance, along with the other laser properties detailed in Table III, informed the calculation of a laser energy range corresponding to an effective LET range in excess of 100 MeV-cm^2/mg, which is sufficient for space applications. The only differences from the SEL to SET scans

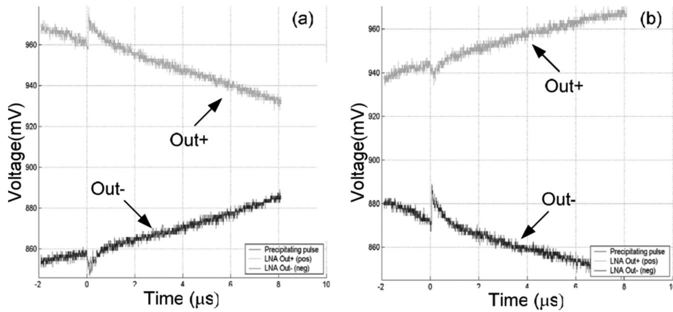

Fig. 14. Onset of output SETs during threshold scan focused on (a) Q_1 and (b) Q_2, according to lacation map in Fig. 18. Target device determines transient amplitude but signal phase determines polarity.

were the decrease in spot diameter, from 30-μm to 1.2-μm and a corresponding increase in effective filter absorbance.

For all scans the LNA was nominally biased, programmed for a worst-case gain of 20dB, and driven by a 10-kHz, 25-m V_{pp} sinusoid, while monitoring its supply and outputs.

B. SEL Performance

The entirety of the die, including the pad ESD cells, was scanned with various blends of laser properties to examine its sensitivity. Regardless of die location, beam intensity, or spot size, the supply was free of glitches, oscillations, or droop. Further, the part remained stable, with no signs of saturation. No latchup or permanent damage was detected up to the maximum beam energy, 1.3 nJ, for spot sizes up to 700 μm^2.

C. SET Performance

The general procedure for SET examination involved: probing a critical transistor array with a narrow diameter spot; increasing the beam intensity to an 'onset threshold', at which point transients of sufficient amplitude could be observed; then, augmenting the intensity by $\sim 3\times$ (high-LET) to note its impact on the transient delay, amplitude, and recovery time.

Consider the alternate application of this methodology to each element the Q_1/Q_2 array of Fig. 8. By depositing charge inside the guard rings, we circumvent their SET protection. Additionally, since device sizing prevented a fully common-centroid layout, this array does not take advantage of the preferred electric-field symmetries in Fig. 9. Finally, since the input pair is biased at a low current density to improve input impedance, we expect a low onset threshold.

The resulting transients from the threshold scan of this array (Fig. 14) are triggered at a laser energy of 22 pJ. Even though only one device is illuminated, the stray drift fields sweep some of the deposited charge into the neighboring device, resulting in a transient on the 'other' side of the circuit that is $1/2$ to $2/3$ as large as its counterpart. Further evidence of the inter-device fields is implied by the transient polarities, which in this and other low-beam-strength cases (<57 pJ) are correlated with the phase of the input signal rather than the target device. That is, the positive-going transient always occurs on the side of the circuit where the sinusoid is in its negative half-period. Notably, the transient amplitudes were insensitive to increase in beam energy beyond the threshold.

TABLE IV
SET STATISTICAL SUMMARY

SET Property	Scan Type	Average	Maximum	Units
Amplitude	Threshold	10-25	40	mV
	High-LET	75-100	400	mV
Recovery Time[a]	Threshold	1-1.5	4	μs
	High-LET	2-2.5	8	μs

High-LET scans are those in which the beam energy exceeds 57 pJ.
[a]Recovery time is measured from onset edge to settling within 1%.

No irrecoverable upsets, oscillations, or saturation were induced. For all arrays scanned, the outputs remained BIBO stable with exponential recovery times, except for slewing noted at extremely high energies. The statistical characteristics for the set of observed transients are summarized in Table IV.

VI. CONCLUSION

We have validated the utility of a class of architectural, implementation-level, and layout-based hardness-by-design techniques by illustrating the robust TID and SEE performance of a wideband, linear, low-power LNA to γ-ray, ^{60}Co, and pulsed-laser irradiations. In addition to a higher performance version of the prototype, future work will examine the morphological discrepancies in the SEE data, explain the measured pMOS ΔV_{th}-vs-dose slope, and develop statistically significant sample sets to track the reported behaviors as a function of LNA gain and process variation.

ACKNOWLEDGMENT

The authors would like to thank National Semiconductor Corporation for fabrication of the prototype chip, and in particular acknowledge the aegis of A. Bahai, and the guidance of S. Khosrowbeygi and J. Shibley. The authors also thank R. Koga, D. Mabry, M. Turpin, B. Garrett, and S. Brown at the Aerospace Corporation for their expertise and rapid problem solving over the course of the radiation testing. Finally, the authors gratefully acknowledge C. Wang and K. Lee of Stanford University for their invaluable technical advice and assistance.

REFERENCES

[1] U. S. Inan, T. F. Bell, J. Bortnik, and J. M. Albert, "Controlled precipitation of radiation belt electrons," *J. Geophys. Res.-Space Phys.*, vol. 108, no. A5, pp. 1186–, May 2003.

[2] R. B. Horne, "Wave acceleration of electrons in the Van Allen radiation belts," *Nature*, vol. 437, no. 7056, pp. 227–30, Sept. 2005.

[3] D. M. Fleetwood, P. S. Winokur, and P. E. Dodd, "Overview of radiation effects on electronics in the space telecommunications environment," *Microelec. Reliab.*, vol. 40, no. 1, pp. 17–26, Jan. 2000.

[4] D. A. Gurnett, "Principles of space plasma wave instrument design," *Measurement Techniques in Space Plasmas: Fields, Geophys. Mono*, vol. 103, pp. 121–136, 1998, R. Pfaff, J. Borovsky, D. Young, Eds., Washington, DC: AGU, Copyright 1998 by American Geophysical Union.

[5] T. F. Bell and R. A. Helliwell, "The Stanford University VLF wave injection experiment on the ISEE-A spacecraft," *IEEE Trans. Geosci. Electron.*, vol. GE-16, no. 3, pp. 248–252, July 1978.

[6] D. A. Gurnett, R. L. Huff, and D. L. Kirchner, "The wideband plasma wave investigation," *Space Sci. Rev.*, vol. 79, pp. 195–208, 1997.

[7] D. A. Gurnett and U. S. Inan, "Plasma wave observations with the dynamics explorer-1 spacecraft," *Rev. Geophys.*, vol. 26, no. 2, pp. 285–316, May 1998.

[8] M. J. Deen, S. Rumysantsev, R. Bashir, and R. Taylor, "Measurements and comparison of low frequency noise in npn and pnp polysilicon emitter BJTs," *J. Appl. Phys.*, vol. 84, no. 1, pp. 625–633, July 1998.

[9] J. A. Babcock, B. Loftin, P. Madhani, X. Chen, A. Pinto, and D. K. Schroder, "Comparative low frequency noise analysis of bipolar and MOS transistors using advanced complementary BiCMOS technology," in *Proc. IEEE Custom Int. Circuits Conf.*, San Diego, CA, 2001, pp. 385–388.

[10] D. M. Fleetwood, T. L. Meisenheimer, and J. H. Scofield, "$1/f$ noise and radiation effects in MOS devices," *IEEE Trans. Electron Devices*, vol. 41, no. 11, pp. 1953–1964, Nov. 1998.

[11] J. D. Cressler, "On the potential of SiGe HBTs for extreme environment electronics," *Proc. IEEE*, vol. 93, no. 9, pp. 1559–1582, Sept. 2005.

[12] J. A. Babcock, "Ionizing radiation tolerance of high-performance SiGe HBTs grown by UHCV/CVD," *IEEE Trans. Nucl. Sci.*, vol. 42, no. 6, pp. 1558–1566, Dec. 1995.

[13] P. R. Gray, P. J. Hurst, S. H. Lewis, and R. G. Meyer*, Analysis and Design of Analog Integrated Circuit*. New York: Wiley, 2001, ch. 8.

[14] A. P. Brokaw and M. P. Timko, "An improved monolithic instrumentation amplifier," *IEEE J. Solid-State Circuits*, vol. SC-10, no. 6, pp. 417–423, Dec. 1975.

[15] R. R. Troutman*, Latchup in CMOS Technology: The Problem and Its Cure*. Norwell, MA: Kluwer, 1986.

[16] A. Hastings*, The Art of Analog Layout*, 2nd ed. New York: Prentice-Hall, 2005, ch. 4, 7.

[17] S. C. Witczak, R. C. Lacoe, J. V. Osborn, J. M. Hutson, and S. C. Moss, "Dose-rate Sensitivity of Modern nMOSFETs," *IEEE Trans. Nucl. Sci.*, vol. 52, no. 6, pp. 2605–2608, Dec. 1995.

[18] Ionizing Radiation (Total Dose) Test Procedure, MIL-STD-883F, Method 1019.6 2003.

[19] M. R. Shaneyfelt, "Impact of passivation layers on ELDRS and pre-irradiation elevated temperature-stress effects in bipolar ICs," *IEEE Trans. Nucl. Sci.*, vol. 49, no. 6, pp. 3171–3179, Dec. 2002.

[20] S. Buchner, "Pulsed laser-induced SEU in integrated circuits: A practical method for hardness assurance testing," *IEEE Trans. Nucl. Sci.*, vol. 37, no. 9, pp. 1825–1831, Dec. 1990.

[21] R. Koga, "Observation of single event upsets in analog microcircuits," *IEEE Trans. Nucl. Sci.*, vol. 40, no. 6, pp. 1838–1844, Dec. 1993.

[22] S. C. Moss, "Correlation of picosecond laser-induced latchup and energetic particle-induced latchup in CMOS test structures," *IEEE Trans. Nucl. Sci.*, vol. 42, no. 6, pp. 1948–1956, Dec. 1995.